Fabrication, test and performance of very large X-ray CCDs designed for astrophysical applications

H. Soltau[a,b], J. Kemmer[a,b,*], N. Meidinger[b,c], D. Stötter[b,c], L. Strüder[b,c], J. Trümper[c], C.v. Zanthier[a,b], H. Bräuniger[c], U. Briel[c], D. Carathanassis[b,d], K. Dennerl[c], S. Engelhard[d], F. Haberl[d], R. Hartmann[d], G. Hartner[c], D. Hauff[b,d], H. Hippmann[c], P. Holl[a,b], E. Kendziorra[e], N. Krause[b,c], P. Lechner[a,b], E. Pfeffermann[c], M. Popp[b,c], C. Reppin[c], H. Seitz[b,d], P. Solc[d], Th. Stadlbauer[b,c], U. Weber[a,b], U. Weichert[a,b]

[a]*KETEK GmbH, Am Isarbach 30, 85764 Oberschleißheim, Germany*
[b]*MPI-Halbeiterlabor, Paul-Gerhardt-Allee 42, D-81245 München, Germany*
[c]*Max-Planck-Institut für Extraterrestrische Physik (MPE), München-Garching, Germany*
[d]*Max-Planck-Institut für Physik (MPI), München, Germany*
[e]*Astronomical Inst. of the Univ. Tübingen (AIT), Tübingen, Germany*

Abstract

A $6 \times 6\,cm^2$ large X-ray CCD has been developed and fabricated at the Semiconductor Laboratory of the Max-Planck-Institut für Extraterrestrische Physik. The CCD has been designed for the focal plane cameras of two satellite missions. The concept is a fully depleted pn-CCD which is sensitive over the whole wafer thickness of about 300 μm. It has been especially developed for X-ray detection delivering a high quantum efficiency over the energy range between 0.2 and 15 keV. A production yield of 27% was achieved. Seven good (almost) defect-free wafers were produced within the performance requirements, i.e. for temperatures below 180 K they show a homogeneous noise level smaller than $5\,e^-$, a uniform spectral response with an energy resolution of 130 eV for Mn-K_α and a reduction of the sensitive area due to defects by less than 0.3%. Three CCDs have now been integrated in the flight cameras. The presentation comprises special aspects related with the fabrication of very large CCDs, a summary of the performance parameters and results of the qualification procedure of the European and German Space Agencies.

1. Introduction

Several X-ray observatories for astrophysical investigations are scheduled for launch in the next two years: AXAF (USA) [1] and ABRIXAS (Germany) [2] in spring 1999, XMM (ESA) [3] in early 2000, ASTRO-E (Japan, USA [4] and JET-X on Spectrum-Gamma-X (Russia) [5] in later 2000.

All focal plane detectors of those satellite missions comprise charge coupled devices (CCDs) as imaging spectroscopic detectors with timing information of the incident X-rays. The scientific

requirements include beside best possible spectral resolution and quantum efficiency from 0.2 keV up to 15 keV, a non-obstructed, homogeneous large field of view, in the order of 40 cm^2. In most of the X-ray instruments, MOS-type CCDs derived from optical devices with monolythic active areas up to $2.5 \times 2.5\ cm^2$ are assembled. They show the good features of the well-established CMOS fabrication process such as small pixel size and low readout noise, but also the disadvantages like the poor sensitive thickness at the lowest and highest energies, and slow readout speed.

One attempt to overcome the constraints resulted in the development of very large pn-CCDs. They are designed and fabricated, with a size of $6 \times 6\ cm^2$, at the Semiconductor Laboratory of the Max-Planck-Institut für Extraterrestrische Physik (MPE). The CCDs are dedicated for two of the above-mentioned satellite missions: One is the European X-ray Multi Mirror mission (XMM), the second cornerstone of ESA's Horizon 2000 program, and the other is the German ABRIXAS project (A BRoad bond Imaging X-ray All-sky Survy). XMM's objective is imaging and spectroscopy of X-ray stars, also faint objects, with good spatial and high energy and time resolution. ABRIXAS' primary goal is an all sky survey. It can be seen as a pathfinder for the XMM mission.

The CCD concept is a fully depleted pn-CCD which is sensitive over the whole wafer thickness of about 300 μm. The basic concept and layout of the detector have been presented in preceding European Symposia on Semiconductor Detectors [6,7]. Its design is deduced from the reverse-biased pin-diode obeying the principle of sideward depletion of a silicon drift chamber. The illumination takes place from the back-side through a homogenous thin entrance window. By these means — large detection volume and thin entrance window — the quantum efficiency is high over the whole energy range between 0.2 and 15 keV. A first amplification step is integrated on the chip, limiting electronic noise. With a size of $6 \times 6\ cm^2$ the detector presents the world's largest X-ray CCD.

The basic detector concept and the design of the pn-CCD are described in Section 2. In Section 3 the fabrication conditions and quality assurance steps related with the production of very large devices are discussed. The testing of the CCDs is described in Section 4. Yield and its limiting factors are outlined in Section 5. The performance of the CCDs, especially homogeneity aspects, is presented in Section 6. Three CCDs have now been integrated in the flight cameras for XMM and ABRIXAS. They have started their final calibration procedure in Panter, the large X-ray test facility at Neuried [8], and at the monochromatic light sources of the synchrotons in Orsay [9] and at BESSY [10]. Section 6 includes first results of the qualification procedures. We conclude with an outlook for future projects and activities in Section 7.

2. Design

The pn-CCD has a size of $6 \times 6\ cm^2$. A top view is shown in Fig. 1. The pixel size is $150 \times 150\ \mu m^2$; it has been adapted to the spatial resolution of the telescope. There is a change in transfer direction in the middle of the CCD, limiting the number of transfers in each channel to 200 pixels. There are 384 channels on each side of the CCD. Every channel is terminated by an anode and an on-chip amplification stage. The amplification is performed by a single-sided n-channel JFET, accompanied by an additional one for resetting the anode. A circular structure has been chosen for the JFETs with regard to radiation hardness. From the on-chip

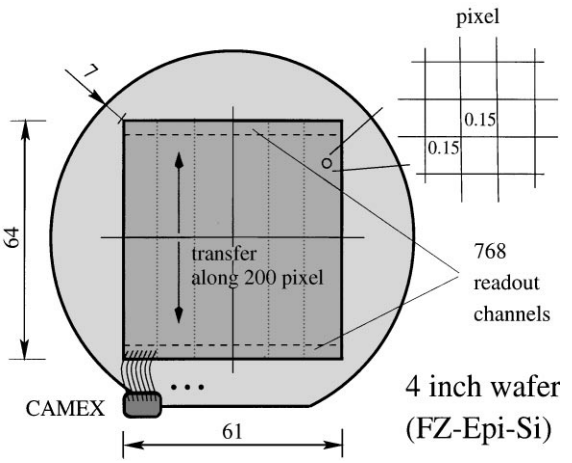

Fig. 1. A schematic drawing of the pn-CCD.

electronics the signals of each row are fed in parallel into a CAMEX64B chip for additional amplification, shaping, sampling and multiplexing [11]. The CAMEX output is sent to a 12-bit 10 MHz ADC. The parallel processing of the signals permits a readout time of 22.5 μs per row.

The pn-CCD is a device fully depleted over the wafer thickness of 300 μm. It is fabricated on high-purity 4 in FZ silicon material with a resistivity of 5 kΩ cm and an epilayer with a resistivity of 40 Ω cm. Fig. 2 shows a cross section of the CCD. The device is sideward depleted by applying a positive voltage to the n^+-anode and negative voltages to the p^+-implantations at the front- and the back-side. The ratio of the negative voltages and the doping levels determines the depth of the transfer channel. It is currently arranged 12 μm below the surface close to the epi/bulk interface.

X-ray photons are entering the detector through the homogeneous thin entrance window at the back-side of the CCD. They are converted to electron–hole clouds at a depth in the wafer following the absorption curve in silicon. While the holes are absorbed at the back-side the electrons are drifting very fast, within 1 ns, in a small cloud towards the transfer channel. The conversion depth within the silicon determines the charge collection efficiency: electrons generated very close to the entrance window, as typical for low X-ray energies as that of carbon, have a certain risk to be partially trapped at the back-side silicon oxide interface.

The average size of the signal charge cloud in the transfer region is 10 μm. Hence most events, about 70%, are single pixel events only; split events do not cover more than a four pixel area. The electrons are collected under the most negative register of each pixel. Three registers are comprising one pixel. They are divided by oxide layers. During readout an appropriate voltage pulse sequence applied to the registers shifts the electrons through the channel notch towards the anode. The channel notch is about 10 μm wide. It is established by deep phosphorous implantations and amplified by a deep boron implant in the channel stop area.

As the CCD has been designed for 10 yr of operation in orbit, redundancy was an important factor in the design. Therefore, the rear-side of the CCD has been devided into four and the front-side into 12 parts with individual independent voltage supplies (see Fig. 1).

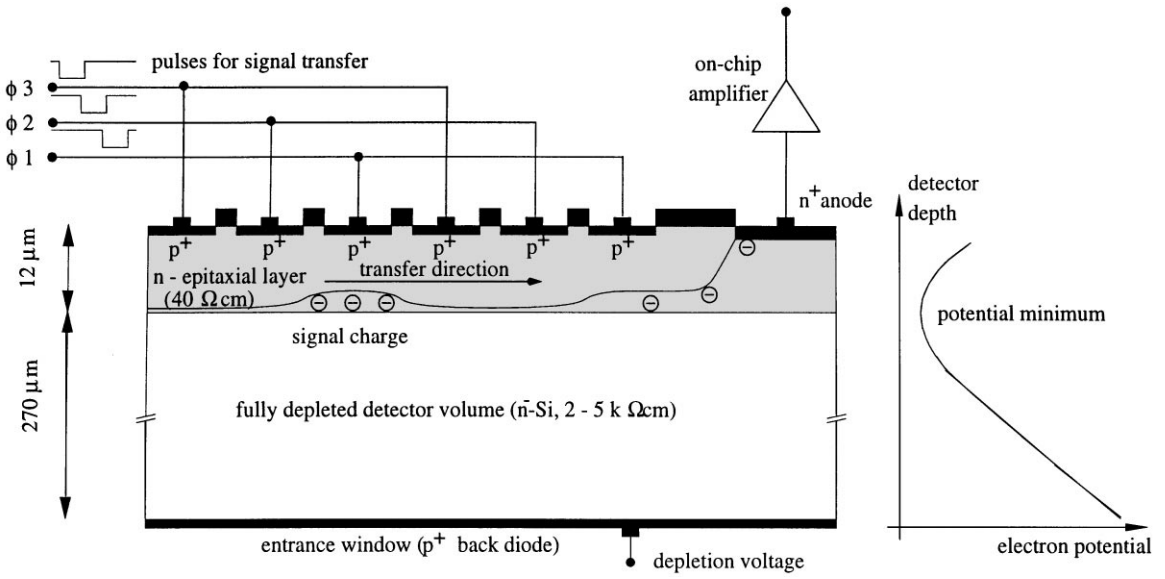

Fig. 2. Cross section through the pn-CCD along a transfer channel.

3. Fabricating very large X-ray CCDs

The task of fabricating (almost) defect-free devices with a sensitive volume of $6 \times 6 \times 0.03\ \mathrm{cm}^3$ is ambitious. It can be achieved either by keeping the number of process wafers large or by improving the individual wafer yield. For a small laboratory the second way is much more effective.

The Semiconductor Laboratory of the Max-Planck-Institute of Extraterrestrical Physics has a clean room area of about 150 m^2 of class 10–100. Standard CMOS technologies are available as oxidation, annealing and tempering, photoresist deposition, proximity mask aligning with a minimum gap and line width of about 3 μm, wet etching and cleaning in benches or sprayers, nitride, oxide and polysilicon LPCVD processes and aluminum sputtering and evaporation. Due to the risk of radiation damage plasma processes are not integrated in the fabrication process till now. Implantation dopings are performed externally. As the CCD is patterned and implanted on both wafer sides all machines in the laboratory have been adapted to double-sided processing. The inner part of the wafer is never touched, a feature crucial for high yield.

The CCD process comprises 15 mask steps. After thermal oxidation and the patterning of the oxide layer diverse implantations and annealing steps follow. The process is finished by the deposition and structuring of nitride and oxide isolating layers as well as aluminum sputtering, structuring and alloying.

For achieving a high wafer yield we introduced the following fabrication requirements in the process:

- a good redundancy in the technological design,
- a low particle density level, at least cleanroom class 10 in the lithography and furnace area,
- avoiding contamination problems,
- thorough wafer cleaning (RCA) before all furnace processes,
- extremely careful processing paying attention to each individual wafer
- rigorous quality assurance measures like
  - the introduction of numerous optical inspections,
  - SIMS measurements of all relevant implants before and after annealing,
  - recurrent control of refraction index and thickness of the isolating layers,
  - temperature profiling and testing of furnaces prior to processing,
- a deep comprehension of the device functional principles and the relevant defect mechanisms,
- very strict rejection rules,

Even small inaccuracies in the photolithography or etching steps were repaired. In the following some examples are presented:

- After thermal oxidation and its first patterning crystal defects of the starting material can be clearly detected by optical inspections in a microscope. We observed epitaxial stacking faults (ESF) with a density of about 0.3 per wafer.

  All wafers with ESFs were excluded from further processing. Crystal defects lead to locally high generation current appearing as bright or very noisy pixel even at low temperatures ($T < 200$ K).
- The thermal oxide layer is structured in our laboratory by wet processing in a spray developer and etcher. Consequently 100% homogeneity cannot be guaranteed. Therefore, detailed optical inspections on each wafer after the developing and the etching process have been performed.

  All inaccuracies down to a size of 2 μm leading to oxide remnants or holes were repaired by spot resist covering or exposure. As, for example, oxide remnants in the register area lead to imperfect boron implantations disturbing the potential distribution of the transfer channel and hindering the complete transfer of the signal charges at this location.
- We had one severe problem during fabrication, that was the nitride LPCVD process. Unfortunately, there were quire a large number of particles which were created and deposited on the wafer in the beginning of the nitride CVD process. There were between 10 and 50 particles on each surface with a size smaller than 3 μm and about 2–10 particles with a size larger than 3 μm ranging up to 10 μm. Many efforts, including megasonic cleaning in SC1 solution or immediate nitride etch after deposition, were made to get rid of the particles, but none was successful.

The nitride particles cause severe problems: As they are very porous and their height is about the same as their diameter they cannot be covered satisfactorily by low-temperature oxide (LTO) (≈ 100 nm) or resist (≈ 1 μm) layers. So etching occurs under the particle in the LTO and nitride structuring steps. During aluminum deposition the metal penetrates the particle and stays there, also after the metal etching step. Taking into account the tendency of aluminum for spiking through oxide or nitride pinholes into the silicon the particles can create short circuits.

The preceding experiences with productions have shown that nitride particles, deposited on the front-side of the CCD on the boarder between a register and its adjacent oxide layer, lead to short circuits between the MOS and the register with a probability of about 30%. Accordingly all these defects were isolated from the aluminum line on the oxide by spot exposure during aluminum patterning. By this method we were able to completely eliminate oxide/register short circuits.

However, nitride particles on the rear entrance window could not be neutralized. With a probability of 30% large particles lead to locally high-generation currents affecting 1–10 pixels, surrounded by a visible and/or infrared light halo.

In Fig. 3 the effect of the defects on the CCD performance is visualized.

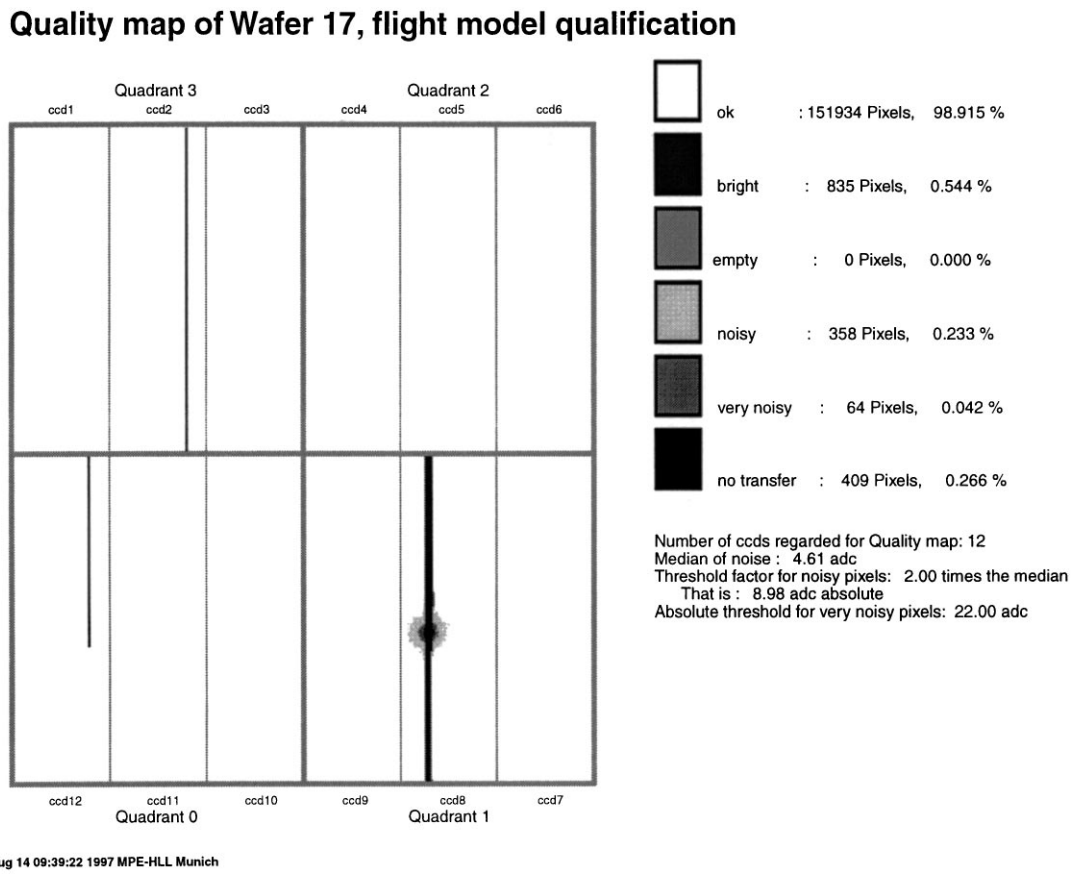

Fig. 3. This wafer was disqualified as flight model due to a bright pixel area and a light spot in Quadrant 1 which has its origin in a nitride particle embedded in the oxide of the entrance window. In Quandrant 0 a bad transfer point is observed and a noisy channel occurs in Quadrant 3.

4. Electrical and spectroscopic performance tests

The first tests of the processed CCDs are electrical DC-measurements at a standard probe station at room temperature. For CCDs which pass this test short circuits and enhanced currents can be excluded. Leakage current is required to be smaller than 30 nA/cm^2 on all rectifying junctions up to a depletion depth of 300 μm.

The electrical qualification step is passed successfully by more than 90% of the CCDs. The second qualification step is a real performance test. The spectroscopic performance as well as the noise level of each individual pixel are determined for the standard operation temperature range between 140 and 200 K. For this purpose a cold-chuck probe station (CCPS) was developed in cooperation with the Suess company [12]. At this probe station the CCD is cooled down to about 150 K by a chuck flushed with nitrogen. The measurement unit is built into a dark box, because any small gleam of light will be registered by the CCD and disturb the performance values. Tow prevent condensation of humidity on the CCD the whole measurement takes place in a dry nitrogen atmosphere. To illuminate the CCD an ^{55}Fe source is deposited above the CCD surface.

The probe card at the CCPS is equipped with the complete CAMEX readout electronics. The signal data are transferred to a 12-bit 10 MHz ADC which delivers data for the computer for online analysis of noise level, intensity map, amplification factor, charge transfer efficiency, split distribution and energy resolution. All voltage can be tuned individually, all currents are measured. By these means and the help of the online software package the optimum operation conditions of each CCD are determined. Of course all data are registered to be analyzed in more detail, offline. It is this procedure which leads to the final qualification of the CCD.

5. Yield

Between 1995 and 1997 six batches have been processed resulting in a total number of about 100 wafers. In 1995 we started with an yield of 0% and ended up in 1997 with an yield of 27%. That means that 27% of the CCDs show performance values which lie within the specifications summarized in Table 1. The specifications refer to standard operation conditions (i.e. essentially 140 K $< T <$ 180 K). They have been adapted to the requirements of the European Space Agency (ESA). The devices show similar and stable operation parameters.

The reason for the zero yield in the beginning was a small defect in one photolithography step which stayed undetected during fabrication. It damaged all wafers on the same spot and ruined the wafer yield completely. As a consequence the fabrication rules listed in Section 4 were introduced. Especially the accuracy in the individual wafer treatment was enhanced significantly. By these means we were able to increase the yield to 27%.

That is not the unsystematic error limit. The yield was dominated by the weakness in the nitride CVD process as described in Section 4. The particles deposited right in the beginning of the CVD process on the entrance window lead to locally unacceptable high generation currents, with an average density of 1.5 per wafer. Before starting a new production the elemination of this problem is a first essential.

Ignoring the defects created by nitride particles we recalculated the yield and found a value of 70% — a number which is now dominated by unsystematic errors.

Overall seven good wafers were produced with CCDs within the requirements. Three CCDs have

Table 1

Area loss	
Due to defects	$< 0.3\%$
Noise level	$4.5e^- – 5.0e^-$
Energy resolution	130–150 eV (Mn K_α) (full frame mode)
Quantum efficiency	$> 60\%$ (200–10 keV) $\approx 80\%$ (275 eV) $\approx 90\%$ (10 keV)
Spatial resolution	120 μm resp. 35 μm (rms)
Time resolution	< 80 ms (full frame mode) ≈ 50 μs (burst mode)
Homogeneity in all performance parameters	
Radiation hardness up to 2×10^9 cm^{-2} protons	

now been integrated in the XMM and ABRIXAS-Cameras, as flight and as flight spare models. They have meanwhile seen all of the ESA and MPE qualification steps.

6. Performance

A first summary of performance is given in Table 1. A detailed discussion is found in Ref. [13] where the results from 1×3 cm^2 large CCDs with identical layout have been presented. The 6×6 cm^2 large CCDs meet these performance values. Selected information is summarized in the following including recent improvements.

6.1. Electronic and system noise, dark current

The equivalent noise charge of the pn-CCD detector system is smaller than $5e^-$ for an integration time of 80 ms and a readout time of 0.35 μs per pixel. the noise shows neglegible temperature dependence between 120 and 190 K, reflecting that dark current is small. The largest noise contributions arise from the CAMEX and electronic pick-up.

6.2. Spatial uniformity

The spatial uniformity in the CCD performance is excellent. With the exception of the areas where the nitride particles created generation centers, the wafers showed homogeneous noise distribution and uniform spectroscopic behavior. The variation in the energy resolution over the whole CCD is smaller than 2% rms as calculated for an Mn–K spectrum. For 27% of the wafers less than 0.3% of the CCD surface were diminished in their performance due to point defects; one wafer showed not a single point defect. These are individual noisy or bright pixels or high charge transfer losses in an isolated pixel, see e.g. Fig. 3. Fig. 4 demonstrates in an intensity plot the homogeneity of the CCD photon efficiency.

6.3. Charge splitting

The effect of charge splitting is much less pronounced for the pn-CCD as for conventional CCDs due to the comparable large pixel size and the strong drift field over the whole detection volume. A percentage as high as 70 of the photons shows up as single events, only 2% split in three or four pixels. This is true for high and low energies. Summation of the split events is possible with good success.

6.4. Quantum efficiency

The pn-CCD has the advantage to be illuminated from its unstructured back-side yielding a homogenous entrance window for all incoming photons. The quantum efficiency is excellent over a wide energy range.

For high-energy photons with large absorption lengths the quantum efficiency is determined by the extension of the sensitive volume. For the pn-CCD it is in accordance with the wafer thickness of 300 μm. For 15 keV photons a sensitivity larger than 50% is achieved.

For low-energy photons with small absorption lengths the quality of the entrance window is substantial. A maximum quantum efficiency is achieved by a minimum thickness of light-absorbing dielectric layers, high recombination lifetime and a high drift velocity at the surface. For the pn-CCD the entrance window is made up by a thin oxide layer of about 20 nm, a shallow boron profile of about 200 nm implantation depth and an overlaying low-dose phosphorous doping [7]. The recombination lifetime is large due to the high-purity starting material, ultraclean processing and high-temperature annealing after implantations. The intention of the phosphorous implant is to increase the electrical field strength and hence the drift velocity close to the surface. Its effect on the spectral response is visualized in Fig. 7.

Fig. 5 shows quantum efficiency measurements in dependence of the X-ray energy: The low-energy data were taken at a monoenergetic light source of the synchrotron BESSY in Berlin. The CCD intensity values were compared with those of a calibrated photodiode. The quantum efficiency at carbon (277 eV) is large with 75%. The high-energy data were taken at a monoenergetic light source of the synchrotron in Orsay with the XMM-Flight Model. The CCD intensity values were compared

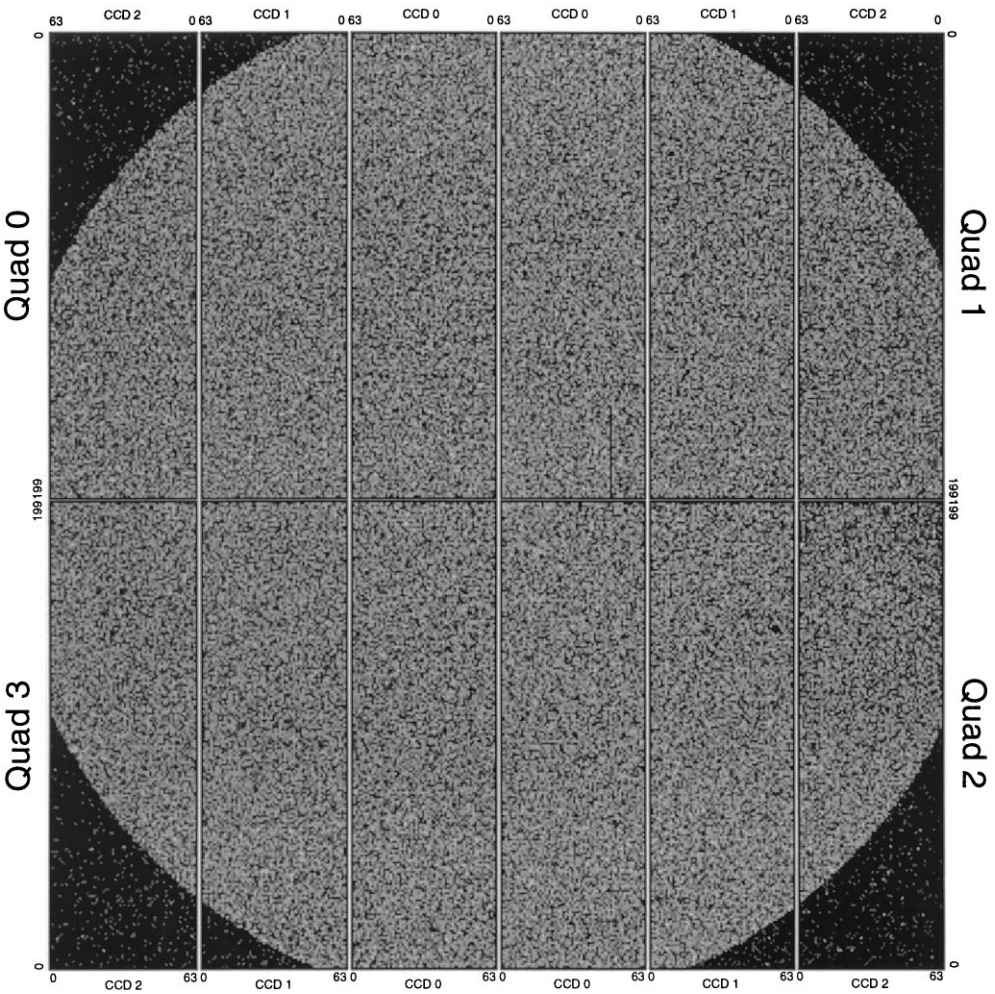

Fig. 4. The CCD shows a uniform spectral response to incoming X-rays.

with those of a calibrated Si(Li) detector. Deviation from 100% efficiency for energies between 2 and 8 keV is ascribed to systematic errors in the calibration setup. The dashed line represents a fit to the data with a two-layer system of silicon oxide and silicon; for more details see Ref. [14].

6.5. *Energy response*

The energy response of the CCD is mainly Gaussian as can be seen e.g. in Fig. 6. The standard deviation is determined by electronic noise, Fano noise and the noise due to statistical fluctuations of the charge transfer from the storing pixel to the anode.

A deviation from the Gaussian form is observed for low-energy photons as demonstrated in Fig. 7. The so-called shoulder in front of the Gaussian peak is due to photons which have been absorbed very close to the entrance window. There the charge collection efficiency is smaller than 1 as parts of the signal electrons are trapped at the Si/SiO_2 interface or at residual recombination centers in the implanted region. Due to the different quality of the Si/SiO_2 interface for $\langle 1\,0\,0 \rangle$ and $\langle 1\,1\,1 \rangle$, CCDs fabricated on $\langle 1\,0\,0 \rangle$ show a better

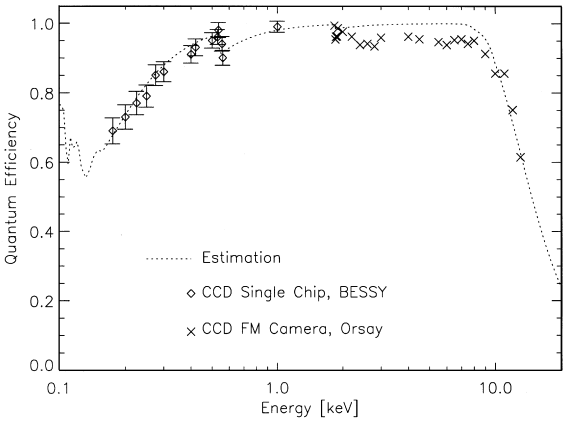

Fig. 5. The CCD shows high quantum efficiency values between 200 and 12 keV.

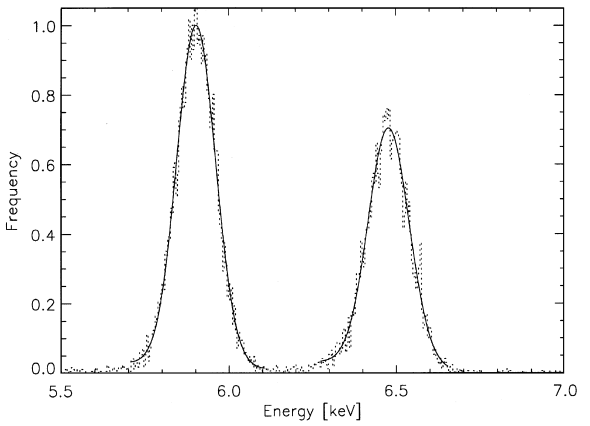

Fig. 6. The spectral response to an ^{55}Fe X-ray source: the energy resolution (FWHM) of the presented Flight Model spectrum is 134 eV at 210 K operation temperature.

low-energy response as clearly demonstrated by Fig. 7. Fig. 8 shows a carbon spectrum for $\langle 1\,0\,0\rangle$ with an energy resolution (FWHM) of 85 eV.

Fig. 9 presents the energy resolution of the detector system with respect to the photon energy. For energies larger than 500 eV the resolution is close to its physical limits. All values are averaged over the whole CCD. The standard deviation is less than 2%. For illustration Fig. 6 shows a Mn K spectrum of the XMM flight model operated at a temperature of 210 K. The energy resolution of the K_α line is as good as 134 eV.

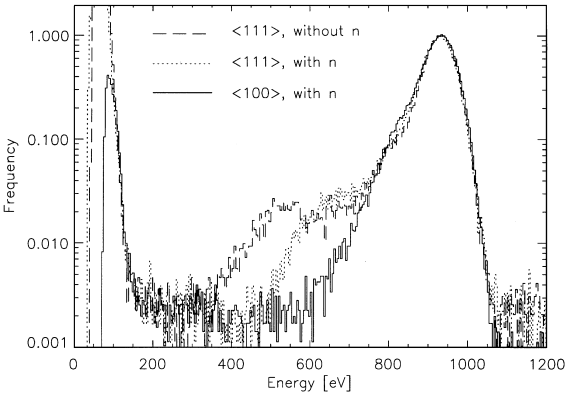

Fig. 7. The spectral response to an Cu-L X-ray source shows a shoulder in advance of the Gaussian peak for $\langle 1\,1\,1\rangle$ material. The shoulder is much less pronounced for $\langle 1\,0\,0\rangle$ silicon. The phosphorous doping (n) improves the detector performance.

Compared with the results presented in Ref. [7] improvements have been made. This is mainly due to an increase of the charge transfer efficiency. The charge transfer efficiency (CTE) is in our case determined by a titanium contamination [15,16].

The raw material is contaminated with titanium during the depostion of the silicon epitaxial layer. It shows enhanced concentration levels, of the order of 10^{10} cm^{-3} up to 10^{11} cm^3, at the bulk/epi interface, close to the transfer region. Introducing a high-temperature annealing into the process improves the CTE. The titanium emerges from the interface getter centers, diffuses through the bulk and is trapped at the boron implant regions or the silicon/silicon-dioxide interface. However, a residual amount remains in the transfer region serving as trapping centers for the signal electrons. Therefore the CTE, and hence the energy resolution, is still determined by the relationship between the temperature-dependent emission time constant of titanium and the readout timing, as indicated in Fig. 10.

6.6. Radiation hardness

Intensive investigations with X-rays (^{55}Fe source, irradiation up to 1.6×10^{12} cm^{-2}), α-particles ^{241}Am source, up to 4.2×10^{7} cm^{-2}) and protons (10 MeV source, up to 1.9×10^{9} cm^{-2})

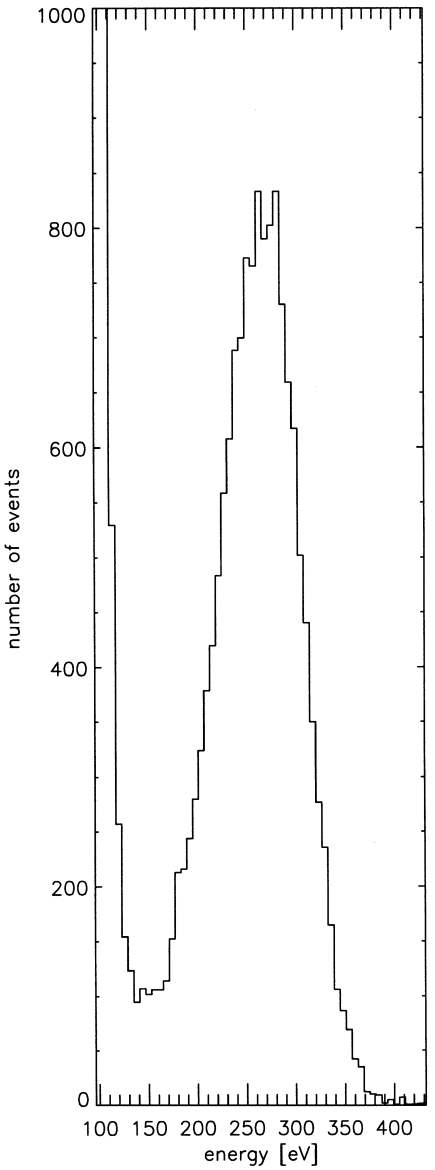

Fig. 8. The spectral response to a carbon X-ray source nearly Gaussian with an energy resolution of 85 eV (FWHM) on $\langle 1\,0\,0 \rangle$ material.

have been made [17,18]. The main results are:

1. No detector failed after any irradiation.
2. No significant increase of dark noise was observed after any irradiation.
3. No change in performance due to X-rays has been registered.
4. For proton and α-particle irradiation A-centers are generated which diminish CTE and consequently decrease the energy resolution. The influence is dependent on operation temperature. For a proton flux as high as 5×10^8 cm^{-2} (10 yr mission of XMM) the energy resolution is only reduced from 145 to 150 eV for Mn K_α at 175 K; for 2×10^9 cm^{-2} according to a 40 yr mission the energy resolution deteriorates to 180 eV.

6.7. Qualification of the flight cameras

Several CCDs have now been integrated in flight camera models for XMM and ABRIXAS. Some models will be used for additional qualification tests (thermo-vacuum, electrical or vibrational tests); three of them, including the spare model, are chosen for operation in orbit. They are calibrated together with the satellite control and communication electronics and the mirrors of the telescope at Panter, the large X-ray facility of MPE, and at monochromatic light sources of the synchrotrons in Orsay and BESSY. Fig. 11 shows the CCD image of a mask illuminated by the light source of the facility of Neuried. The energy resolution of the camera can be compared to the measurement values presented in Figs. 9 and 6. The quality is slightly reduced due to additional noise components of the camera and non-optimum operation conditions in time and temperature, resulting e.g. in a reduction of the energy resolution for Mn K_α to 140 eV. Fig. 5 shows quantum efficiency values as a result of the measurement camapaign in Orsay.

7. Summary and outlook

Almost defect-free very large X-ray CCDs with a size of $6 \times 6 \times 0.03$ cm^{-3} have been fabricated at the Semiconductor Laboratory of the MPE with an excellent performance. An yield of 27% was achieved. It was limited by nitride particles deposited on the entrance window which generated locally high-generation current. Eleminating this problem an yield of 70% would have been possible.

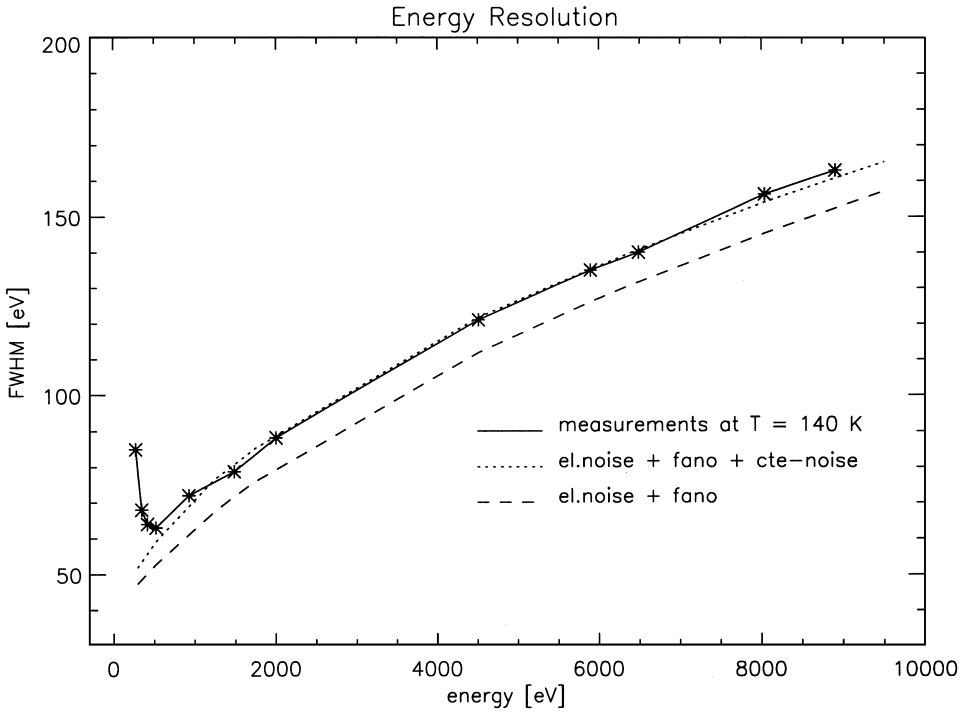

Fig. 9. The energy resolution of the pn-CCD.

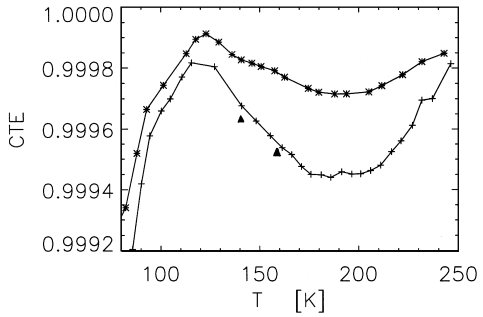

Fig. 10. The charge transfer efficiency (CTE) of the CCD with respect to operation temperature. Cross marks (+ - +) refer to low-temperature and star marks (∗-∗) to high-temperature annealing. The triangles indicate the reduction of the CTE due to the slow XMM-flight timing.

Further X-ray missions require improved focal instruments. Certainly, a straightforward extrapolation of all relevant physical quantities such as position and time resolution, energy resolution, high quantum efficiency and count rate capability, radiation and environmental tolerance, ease of operation, homogeneous, non-obstructed field of view and so forth, cannot be achieved on the basis of the present detector concepts.

The significantly enlarged collecting area of the future X-ray telescopes and the improved angular resolution will require multi-mega pixels systems with the possibility of digesting up to 1000 counts per second and per half energy width of the telescope, typically translating in "frame speed" of the order of a millisecond. Active pixel sensors (APS) will become serious competitors for X-ray CCDs, mainly because they will be able to process the pixel information in the required readout time [19].

Both, improved pn-CCDs with a frame store readout scheme and APS X-ray detectors will be developed in the next years at the Semiconductor Laboratory maintaining the good X-ray properties and improving signal throughout.

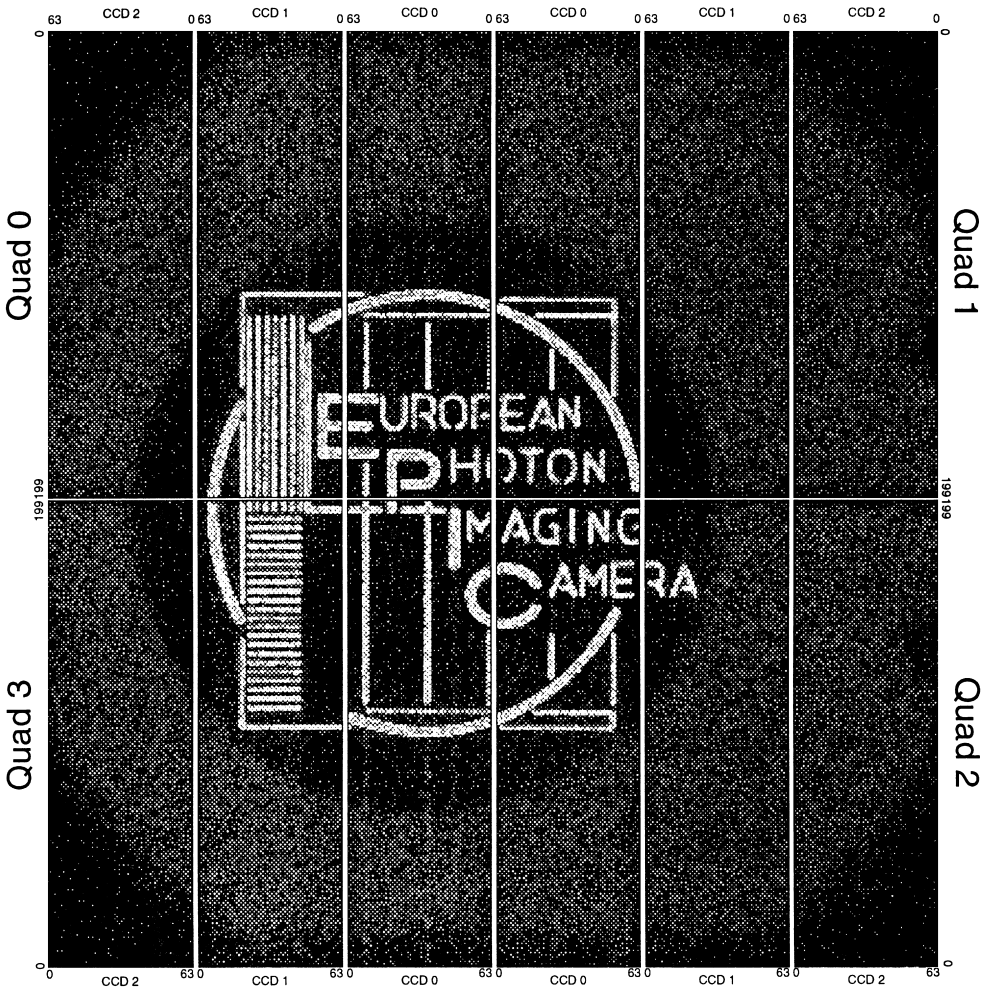

Fig. 11. The EPIC logo of the focal camera consortium of XMM illuminated on the CCD.

Acknowledgements

Funded by BMBF under contract (50-OX-90020/XMM-EPIC) and the Heidenhain Foundation.

References

[1] S.L. O'Dell, M.C. Weisskopf, SPIE 3444 (1998) 2.
[2] P. Friedrich, SPIE 3444 (1998) 342.
[3] D.H. Lumb, H. Eggel, R. Laine, A.J. Peacock, SPIE 2808 (1996) 326.
[4] T. Takahashi, M. Nomachi, Y. Fukazawa et al., SPIE 3444 (1998) 155.
[5] A.A. Wells, C.M. Castelli, M. Denby et al., SPIE 3444 (1998) 392.
[6] H. Bräuninger, R. Danner, D. Hauff et al., Nucl. Instr. and Meth. 326 (1993) 129.
[7] R. Hartmann, P. Lechner, L. Strüder et al., Nucl. Instr. and Meth. 377 (1996) 191.
[8] P. Friedrich, H. Bräuninger, W. Burkert et al., SPIE 3444 (1998) 396.
[9] P. Dhez, E. Jourdain, O. Hainaut et al., SPIE 3114 (1997) 134.
[10] H. Rabus, F. Scholze, R. Thornagel, G. Ulm, Nucl. Instr. and Meth. 377 (1996) 209.
[11] W. Buttler, G. Lutz, V. Liberali et al., Nucl. Instr. and Meth. A 288 (1989) 140.
[12] C.v. Zanthier, P. Holl, J. Kemmer et al., SPIE 3301 (1998) 27.

[13] H. Soltau, P. Holl, J. Kemmer et al., Nucl. Instr. and Meth. 377 (1996) 340.
[14] R. Hartmann, K.-H. Stephan, L. Strüder et al., Nucl. Instr. and Meth. A 439 (2000) 216.
[15] H. Soltau, N. Krause, N. Meidinger et al., Defect induced charge transfer losses in high resistivity float zone silicon charge coupled devices, in: Symposium on High Purity Silicon IV, Vol. 96–13, Electrochemical Society, 1996, pp. 325.
[16] N. Krause, H. Soltau, D. Hauff et al., Nucl. Instr. and Meth. A 439 (2000) 228.
[17] P. Holl, E. Bihler, H. Bräuninger et al., SPIE 3114 (1997) 126.
[18] N. Meidinger, B. Schmalhofer, L. Strüder et al., IEEE Nucl. Sci. NS-45 (6) (1998) 2849.
[19] L. Strüder, Nucl. Instr. and Meth. A 436 (1999) 53.